Dust Directionality and an Anomalous Interplanetary Dust Population Detected by the Parker Solar Probe

A. Pusack[1] ![ORCID], D. M. Malaspina[1,2] ![ORCID], J. R. Szalay[3] ![ORCID], S. D. Bale[4,5] ![ORCID], Keith Goetz[6] ![ORCID], Robert J. MacDowall[7] ![ORCID], and
Marc Pulupa[4] ![ORCID]

[1] Laboratory for Atmospheric and Space Physics, University of Colorado Boulder, Boulder, CO, USA; anna.pusack@lasp.colorado.edu, anna.pusack@colorado.edu
[2] Department of Astrophysical and Planetary Sciences, University of Colorado Boulder, Boulder, CO, USA
[3] Department of Astrophysical Sciences, Princeton University, Princeton, NJ, USA
[4] Space Sciences Laboratory, University of California, Berkeley, CA, USA
[5] Physics Department, University of California, Berkeley, CA, USA
[6] School of Physics and Astronomy, University of Minnesota, Minneapolis, MN, USA
[7] NASA Goddard Space Flight Center, Greenbelt, MD, USA

Abstract

Theory and previous space missions indicate there are several populations of zodiacal dust. The most prominent populations are grains on bound elliptic orbits (α-meteoroids), and β-meteoroids on hyperbolic escape trajectories governed largely by their size and composition. Yet, there may be other populations not yet confirmed by observation. The Parker Solar Probe (PSP) spacecraft is able to observe in situ dust populations in the densest part of the zodiacal cloud. Over the first seven orbits, dust count rates are well organized by orbital groups based on orbital parameters of PSP's shrinking orbit. In particular, the first three orbits and the sixth orbit have a single, preperihelion peak in count rate with a gradual drop off postperihelion, while Orbits 4, 5, and 7 have two distinct count rate peaks on either side of perihelion. The secondary peaks in Orbits 4, 5, and 7 are inconsistent with current zodiacal dust models that account for only two dust populations: α- and β-meteoroids. In examining the directionality of dust impacts on the PSP spacecraft, the presence of an anti-ram impactor anomaly postperihelion during Orbit 4 is evident. This anomaly may indicate another dust population beyond the nominal α- and β-meteoroids, and its origin may be related to the Geminids meteoroid stream associated with the asteroid 3200 Phaethon.

Unified Astronomy Thesaurus concepts: Zodiacal cloud (1845); Micrometeoroids (1048)

1. Introduction

Dust populations near the Sun are historically difficult to study. Observations of the zodiacal cloud (dust grains orbiting the Sun) are ambiguous when line-of-sight (LOS) brightness integration is inverted to determine the cloud properties (Mann et al. 2004). Further, LOS observations require that the size of the dust particles be large for detection (Mann et al. 2004). Exact densities and other properties of the near-Sun dust cloud are thus difficult to determine. So, understanding dust populations near the Sun relies on space-based observations that can make in situ measurements which can detect smaller particles than line-of-sight measurements from Earth (Mann et al. 2004). The in situ measurements are limited, however, to where the spacecraft travels in the solar system, to low count rates, and to narrow fields of view (e.g., Tsurutani et al. 2004; Krüger et al. 2015). Spacecraft have made observations of dust populations using dedicated dust detectors, including Helios (Laakso et al. 1989), while others have used electric field antennas, such as Voyager 2 (Gurnett et al. 1986), DS1 (Tsurutani et al. 2003, 2004), Solar Terrestrial Relations Observatory (STEREO; Meyer-Vernet et al. 2009; Zaslavsky et al. 2012), Wind (Malaspina et al. 2014; Kellogg et al. 2016), and Cassini (Ye et al. 2014). Dedicated dust detectors provide information such as composition and mass, but have a limited collecting area, whereas the electric

field antennas utilize the whole spacecraft area as a dust detector and can register far more events but cannot uniquely determine composition and mass information. Prior studies (Tsurutani et al. 2004) have investigated the possibility of a design that takes the timing of the expansion of an impactor's plasma cloud into account to determine the mass of the impacting particle, but this has not yet been demonstrated in flight. Both methods contribute to understanding the near-Sun dust environment.

Understanding near-Sun dust populations has implications for theoretical astrophysics as well as for aerospace engineering. Detailing how the Sun processes material such as dust grants insight into planetary formation for its own system as well as for extrasolar systems (e.g., Krivov et al. 2000; Dorschner 2001; Grün et al. 2019; Krüger et al. 2019). Further, being able to accurately predict the trajectories of debris in the system helps inform engineers on how to best equip our spacefaring vessels on their various missions (e.g., Grün et al. 2019; McNutt et al. 2019).

Two prominent populations of dust are theorized to be in the inner solar system: dust on bound, elliptic orbits known as α-meteoroids and dust on hyperbolic orbits known as β-meteoroids (Grün et al. 1985). The β refers to the ratio between the force of the Sun's radiation pressure to the Sun's force of gravity: $\beta = F_r/F_g$. For grains on initially circular orbits, a $\beta > 0.5$ results in a particle which is on a hyperbolic trajectory out of the solar system (Zook & Berg 1975; Szalay et al. 2020). Both bound and unbound particles likely have their origins in comets and asteroids that slough off material as they near the Sun (e.g., Koschny et al. 2019). Poynting–Robertson drag pulls in dust

particles from further away toward the Sun, resulting in the highest dust density in the near-Sun environment (e.g., Mann et al. 2004; Koschny et al. 2019 and references therein).

While some spacecraft have been equipped with dedicated dust detectors to capture and analyze dust, other spacecraft have also been able to contribute to the in situ study of heliospheric dust populations, some using electric field instruments. The in situ detection of dust via electric field instruments is well documented for several spacecraft (e.g., Gurnett et al. 1986; Laakso et al. 1989; Tsurutani et al. 2003; Meyer-Vernet et al. 2009; Zaslavsky et al. 2012; Malaspina et al. 2014; Andersson et al. 2015; Kellogg et al. 2016; Vaverka et al. 2018, 2019). Voyager 2 was the first to detect dust impacts via its plasma wave antenna (Gurnett et al. 1986). These antenna were designed to measure the electric potential difference between the spacecraft and the antenna. As Voyager passed through the rings of Saturn and then later through the rings of Neptune, the antenna picked up intense broadband noise that was attributed to dust impacting the spacecraft (Gurnett et al. 1986). To determine that this noise was indeed due to dust impacts, the data were correlated with time series waveform data which showed the general shape of an initial peak with a relaxation back to equilibrium. This impact ionization process indicates that the spacecraft experienced a dust impact. This process has been further documented in space by Cassini (Nouzák et al. 2018; Mann et al. 2019) and studied in the laboratory, (e.g., Collette et al. 2014, 2015, 2016; Shen et al. 2021b and references therein).

The Parker Solar Probe (PSP) mission has three main science objectives: (1) discover the energetic origins of the corona and solar wind, (2) determine the physical structure and dynamics that govern the solar wind, and (3) explore how energetic particles in the solar environment move and evolve (Fox et al. 2016). The PSP mission is to nominally to measure the solar wind, but the electric fields antennas of the FIELDS instrument (Bale et al. 2016) also allow for observations of dust in the near-Sun environment. The FIELDS antennas measure the electric field local to the spacecraft, recording waveforms produced from the dust impact ionization process (Malaspina et al. 2020; Page et al. 2020). Given the proper configuration of the antennas, the location where the impactor hit the spacecraft can be determined, and knowing the directionality constrains the dust population of origin.

To learn about near-Sun dust populations, data from PSP's FIELDS antennas taken in the first seven orbits of the mission are examined. A general pattern of dust detection is evident during these seven orbits, spanning three distinct orbit groups. With a focus on Orbit 4, where single-ended potential data are continuously available for all four electric field antennas in the plane of the heat shield, the data analysis determines the approximate direction of each impactor. Within this data set, unexpected features invite further analysis and may point to an additional localized dust population.

2. Instrument/Data Description

PSP was launched in 2018 and was built to probe closer to the Sun than any previous human-made object. Its planned 24 orbits of the Sun will utilize Venus gravitational assists to progressively reduce its perihelion to about $9.8R_\odot$ (0.046 au). These orbits are subdivided into groups based on orbital characteristics such as eccentricity and perihelion distance (Fox et al. 2016) (see Table 1 for the first three orbital groups explored in this study).

Table 1
Orbital Parameters for Orbits 1–7 as Pertinent for This Study

PSP Orbit Characteristics			
Orbit	a (au)	i (deg)	r_{PH} (au($R_\odot$))	V_{PH} (km s^{-1})
1–3	0.5220	3.361	0.16(36)	95
4–5	0.5021	3.395	0.13(28)	109
6–7	0.4557	3.384	0.095(20)	130

Note. The semimajor axis a in au; the angle of orbit inclination i in degrees; the radial distance of the spacecraft at perihelion r_{PH} in au and solar radii ($R_\odot$); and the speed of the spacecraft at perihelion V_{PH} in kms^{-1} (Szalay et al. 2020).

2.1. FIELDS Electric Field Antennas and Monopole Configuration

The FIELDS suite of instruments measure in situ electric and magnetic fields as well as radio emissions. From these measurements, density fluctuations and spacecraft floating spacecraft potential are also inferred (Bale et al. 2016). In particular, there are five electric field antennas. The electric field antennas are arranged such that four antennas (V1, V2, V3, and V4; Figures 1(a) and (b)) extend in the plane of the heat shield, in a near orthogonal orientation and are generally perpendicular to the spacecraft–Sun line during encounter (i.e., ±1 week from perihelion). Away from encounter, the spacecraft executes maneuvers that roll and tilt away from sunward for thermal management, instrument calibration, and communication with Earth. A fifth, much smaller antenna (V5, not shown) is located on the tail magnetometer boom, near the search coil magnetometer. This study focuses on the data from V1, V2, V3, and V4 ("planar antennas") to determine the directionality of the dust impacting the spacecraft. V5 data require a different interpretation than the scope of this study allows.

The four planar antennas (see Figure 1) can record data in a variety of configurations, but the monopole configuration is most useful for this study. In the monopole configuration, the recorded voltage amplitudes, V_{mono} from the four antenna correspond to the difference in potential between that specific antenna's potential V_i (where i refers to the specific number of the antenna) and the spacecraft potential, V_{SC}: $V_{mono_i} = V_i - V_{SC}$. For example, $V_{mono_2} = V_2 - V_{SC}$. This monopole configuration allows for collecting sufficient quality dust impact data (Ye et al. 2014), and also for determining dust impact direction (Malaspina et al. 2020). All orbits thus far have at least had the V2 antenna in monopole configuration, but Orbit 4 was configured such that all four planar antennas were in the monopole configuration, allowing for a detailed analysis of the rates as well as the directionality of the dust impacts discussed below.

2.2. TDSmax Data

The data used in this study comes from the Time Domain Sampler (TDS) receiver which is configured to record the peak amplitude for each of five input channels in each sampled time window, about 60 s outside of 0.25 au and 6 s during perihelion encounter (Page et al. 2020). These data are found in the TDSmax data product.

Correlated waveform information obtained from the wave burst data in TDS indicates whether any recorded data point is a dust impact. Both Malaspina et al. (2020) and Page et al. (2020) demonstrate that recorded amplitude spikes recorded for
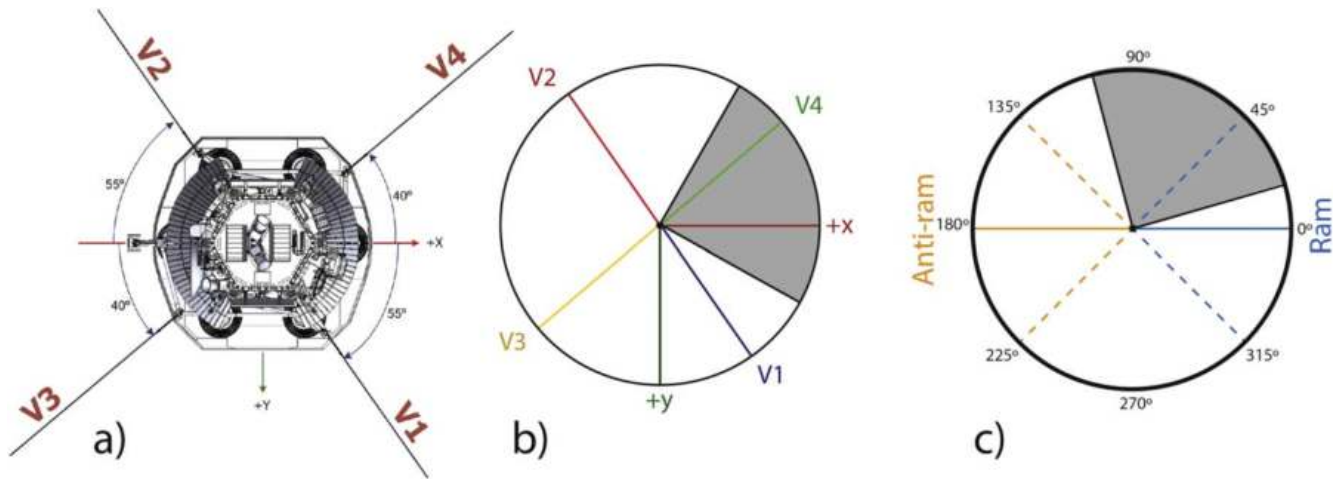
Figure 1. (a) Schematic of PSP with spacecraft coordinates x and y, with $+z$ pointing toward the Sun (into the page). The FIELDS antennas are also shown, with the relative angles between them. (b) Polar plot of a normalized histogram in the spacecraft frame with four colored lines representing the four antennas in the plane of the heat shield. The gray wedge represents the contribution of one dust impact to the polar histogram. (c) Polar plot of a normalized histogram incorporating roll in the system (Sun) frame, with ram corresponding to the spacecraft direction of travel.

Orbits 1, 2, and 3 correspond to dust impacts when the amplitude is above a certain threshold. Page et al. (2020) takes this threshold to be 50 mV, but others (Bale et al. 2020) use 25 mV as a lower limit. This study takes the 50 mV threshold for all analyses, noting that dust detections were found on early orbits above the 50 mV range with a 1% rate of misattribution (Page et al. 2020), that Orbit 4 is in a different orbital group than has been previously analyzed, and that high frequency plasma waves might be included in the 25–50 mV amplitude range.

3. Methodology/Analysis

3.1. Overview Orbits 1–7

Figure 2 shows the dust impact rates as recorded by the V2 antenna (which extends between anti-ram and ecliptic south during perihelion encounter, Bale et al. 2016) in counts per hour in 8 hr time bins of the TDSmax data with a 50–1000 mV amplitude range for the first seven orbits. The orbits are grouped according to orbital parameters (Fox et al. 2016) and this grouping plays out in the shapes of the count rates. Orbits 1–3 have much lower count rate peaks compared with Orbits 4–5 and Orbits 6–7, with the max count rate for the first group found in Orbit 2 at 60.3 ± 2.8 counts hr^{-1}, the peak in the second group found in Orbit 5 with 110.0 ± 3.7 counts hr^{-1}, and the peak rate is found in Orbit 7 at 178.9 ± 4.8 counts hr^{-1}. This shows an 82.5% increase in dust impact count rates between the first and second orbit groups and a 62.6% increase between the second and third orbit groups.

Another aspect to these dust count rates to note is that even within orbital groups, count rates increase. For the initial peaks in each orbit using the 50–1000 mV amplitude bin, there is a 145% increase from Orbit 1 to 2, a 31.5% increase from Orbit 4 to 5, and 36.7% increase from Orbit 6 to 7.

The most striking difference seen in Figure 2 is in the shape of the impact rates plots. Orbits 1–3 show an initial peak before perihelion with no distinct dip at closest approach followed by a gradual decrease in the rates as the craft leaves encounter. Orbits 4–5 exhibit a preperihelion peak, but also show an additional peak after perihelion, with a distinct dip at perihelion. Orbit 6 again shows a preperihelion peak, but the

postperihelion region has a less distinct shape which could either be a shallow peak or a gradual decline as in Orbits 1–3. Orbit 7, then, exhibits a distinct second peak with higher peak rates than any previous orbit.

The first peak for all of these orbits is predicted based on a two-component model of zodiacal impactors (Szalay et al. 2021; e.g., see Figure 4(d) for Orbit 4) and the assumption that the majority of dust particles are in prograde, circular orbits along with the spacecraft (Page et al. 2020; Szalay et al. 2020). Additionally, for a population of grains on circular, prograde orbits, PSP impact rates would be expected to reach a local minimum at close approach. This is due to the local impact speed minimum here due to PSP directly "catching up" with these grains near close approach (Szalay et al. 2020). The impact rates exhibit a local minimum at perihelion for Orbits 4–7 but not in the first three orbits.

3.2. Dust Directionality in Orbit 4

Using TDSmax data and the planar antennas in the monopole configuration for Orbit 4 allows for determination of where on the spacecraft an impact occurred, thus constraining the directionality of the impactor.

An important part of determining the direction of dust impacts is to account for the roll of the spacecraft. Outside of close encounter ($\sim$55 $R_\odot$), the spacecraft rolls about its z-axis (Figure 3). This roll angle is recorded by the spacecraft and is here taken into account to determine dust impact locations outside of perihelion. The spacecraft orientation is fixed when $r_{sc} < 55 R_s$, such that the $+x$ in the spacecraft frame (Figure 1(a)) is in the ram direction (i.e., tangent direction in the system frame). For both pre- and postperihelion counts, there are increases for the V1–V4 group (on the ram side of the craft during encounter) over the V2–V3 group (on the anti-ram side of the craft during encounter): about 25% at peak on the inbound and about 7% at peak on outbound.

The algorithm to determine the direction of dust impact is as follows, adapted from Malaspina et al. (2020):

(1) The data are subdivided into time bins. Here, most of the analysis was conducted using 8 hr time bins, though other size bins were also examined as needed.
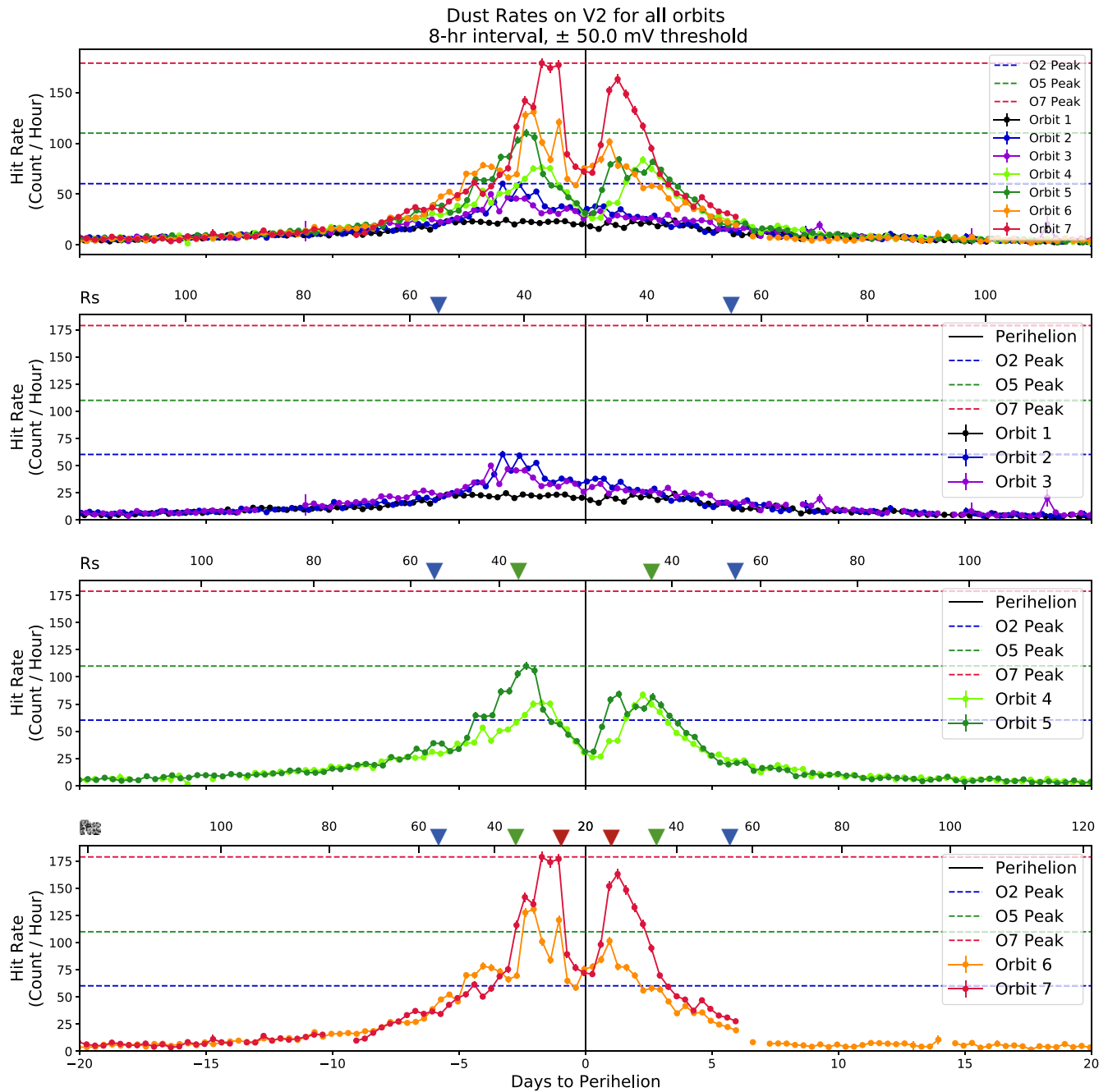
Figure 2. First seven orbits, dust rates (count hr^{-1}) calculated within 8 hr time bins using a ± 50 mV lower threshold and Poisson error calculations, plotted vs. days to perihelion (bottom horizontal axes) and vs. distance in solar radii (R_s, top horizontal axes on panels 2, 3, and 4). Data are from the V2 antenna in monopole mode for each orbit. Black vertical lines indicate respective perihelion, and horizontal lines indicate peak impact rates for each orbital group. Blue carets represent ± 54 R_S, the beginning and end of encounter when there are changes in FIELDS sampling cadences. The green carets represent ± 35 R_S enclosing the section of orbit not covered in Orbits 1–3, and red carets represent ± 28 R_S enclosing the section of orbit not covered in Orbits 1–5.

(2) The largest absolute value amplitude observation is assumed to indicate the closest antenna to the impact, and the second-highest amplitude event corresponds to the second-closest antenna. This assumption is strongly corroborated by laboratory experiments (Shen et al. 2021a). In addition to the lower amplitude limit to ensure a given peak detection is not a plasma wave event, an upper limit is also imposed because the TDS receiver saturates at ~ 1000 mV. If there is one saturated antenna signal, then that antenna is the closest to the impactor, but if there is more than one saturated antenna signal, that dust count is disregarded for the purpose of determining dust

directionality using this method. Further, if the highest amplitude pairs correspond to (V1, V2) or (V3, V4), in either order, that impact is disregarded as those pairs indicate an impactor whose direction cannot be ascertained via this method as those pairs are on opposite sides of the spacecraft. This is generally rare (i.e., $\lesssim 10\%$ of the counts are disregarded), except for several days immediately after perihelion where a maximum of 50% of the counts have the highest amplitudes on opposite antennas.

(3) The most probable impact location is modeled as a 90° wedge in the plane of the heat shield, with an open angle centered on the antenna with the largest recorded amplitude.
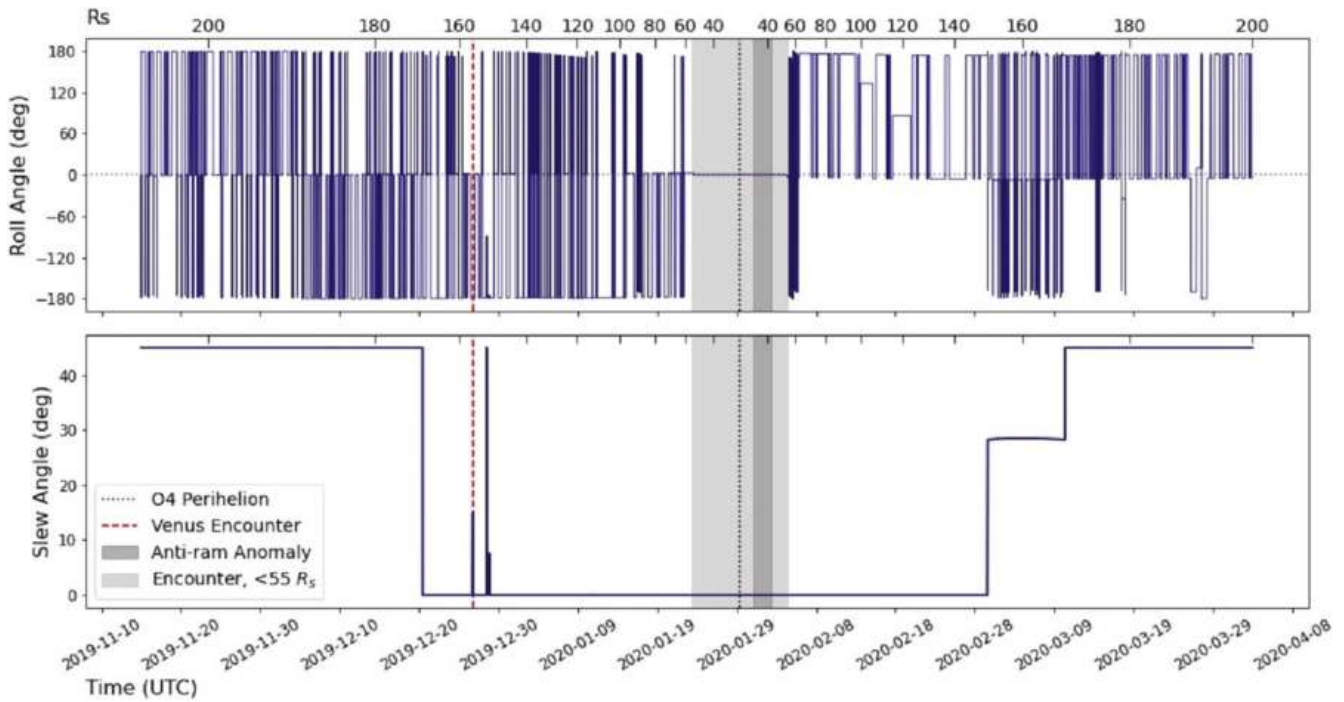
Figure 3. Top: spacecraft roll angle (deg) vs. date (UTC, bottom horizontal axis) and heliocentric distance (R_S, top horizontal axis). Bottom: spacecraft slew angle vs. date and distance. Perihelion is denoted by the black dotted line, encounter by the light gray shading and the anomaly (Section 3.3) period by the dark gray shading.

(4) The 90° wedge is shifted toward the second-highest antenna via the relation

$$\theta_{\text{shift}} = \theta^* \left(\frac{V_{\text{2nd}}}{V_{\text{1st}}} \right),$$

where θ^* is the half-angle between each probe pair, and V_{1st} and V_{2nd} are the monopole antennas with the highest and second-highest recorded amplitudes, respectively (refer to Figure 1(b); e.g., $\theta^* = 95°/2$ between V1 and V4).

(5) To account for the roll of the spacecraft (see Figure 3) about the z-axis in the spacecraft frame outside of 55 R_s, the roll angle is then added to the shifted wedge to shift it further, taking into account whether the craft completes a full 360° spin (Figure 1(c), e.g., if the spacecraft counterclockwise by 30°).

(6) Once this wedge is determined, a value of 1 is added to a histogram bin for pseudo-counts where 0° corresponds to the x_t direction (tangential) in the solar frame, i.e., the ram direction of the spacecraft, and 180° indicates the anti-ram direction in the solar frame (Figure 1(c)).

Each data set is sorted based on the number of counts, requiring that a time interval have counts >75 to be considered statistically significant. Each set is then normalized by dividing by the max value in each set and plotted on a polar plot to create a two-dimensional histogram.

These histograms are examined under a variety of parameters. The histograms are generated using an 8 hr time bin and five amplitude bins (the full 50–1000 mV voltage amplitude range as well as subdivision ranges: 50–100, 100–200, 200–400, and 400–1000 mV). These amplitude bins were chosen to ensure there were enough counts to be considered statistically significant. For full analysis, this process is repeated for 4 and 12 hr time bins as well, allowing for different degrees of analytical depth to probe interesting features in the the data. These subdivisions grant 15 possible combinations to examine the structures observed in the histograms. However, only 11 of

these combinations had >75 counts and so are considered statistically significant.

In general, more low-amplitude than high-amplitude counts are present, so much so that the higher amplitude windows often do not produce statistically significant histograms for all the days in the orbit. The resulting histograms give a rough outline of the direction of dust impacts, with each plot shown as looking on-axis from the spacecraft to the Sun (Figure 4).

A ratio of ram to anti-ram is produced from the histogram data, using $0° \pm 45°$ as ram and $180° \pm 45°$ as anti-ram (defining each as $\pm 90°$ did not offer any appreciable difference in interpretation). In the preperihelion part of the orbit, about a week from closest approach, there is a long period where the ratio is around one, indicating comparable fluxes with the ram and anti-ram surfaces of PSP. This is reflected in the histograms (Figure 4(a)) which show that the spacecraft is bombarded from all angles, though with a moderate number of impacts. The preperihelion count rate peak corresponds to a preperihelion peak in the ram/anti-ram ratio (not shown), signifying a distinct ram preference for impactors as the spacecraft moves through close approach ($< 55R_S$) toward perihelion. At perihelion, a ram preference is again evident (Figure 4(b)), though not as pronounced as in the preperihelion peak. The postperihelion section of Orbit 4 has an interesting phenomenon labeled the "anti-ram anomaly" (Figure 4(c)), which appears as a protruding wedge shape in the anti-ram portion of the histograms, and is discussed in more detail in the next section. This anomalous structure begins in the postperihelion count rate peak and continues as the rates decrease with the spacecraft moving out of encounter. The ram/anti-ram ratio becomes more erratic after encounter ($> 55R_S$).

3.3. Postperihelion Anomaly

The postperihelion anti-ram anomaly appears in the 50–1000 mV amplitude bin on 2020 January 31 at about 4:00
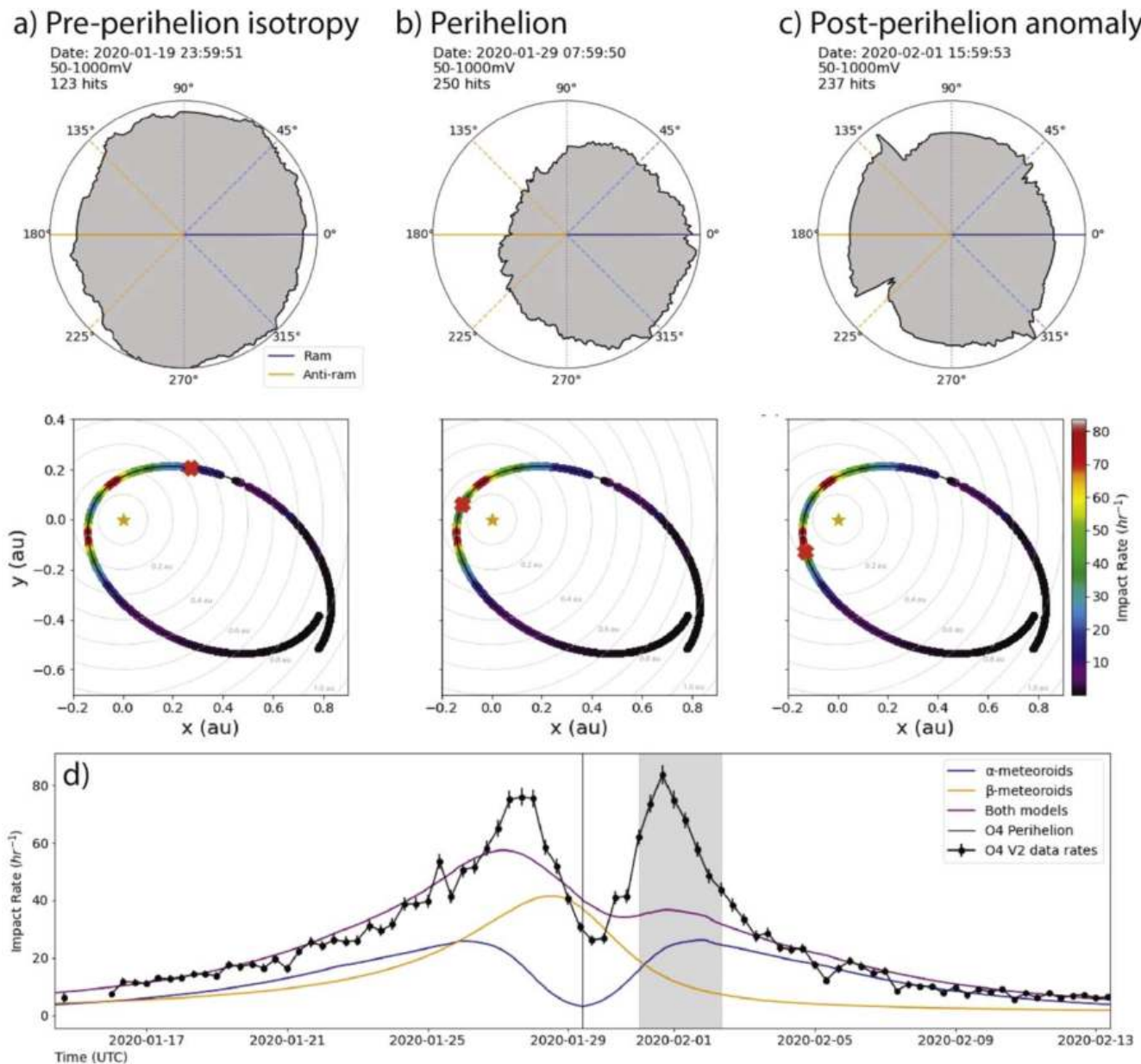
5

Figure 4. Orbit 4 dust impact histograms, using 8 hr time bins and the 50–1000 mV amplitude bin. All counts occurred in time intervals starting at time shown, with time stamp given in UTC. Top Row: polar histograms. Middle row: orbital position with axes in J2000 coordinates with units of au. Far left column (a): isotropic in weeks leading up to perihelion; middle (b): beginning about 2 hours prior to perihelion; far right (c): second peak postperihelion and in midst of anomaly. Bottom Plot: (d): Count rates in data and models. Black indicates the count rates (hr^{-1}) found in V2 data for 50–1000 mV. Solid lines are models for impact rates of α-meteoroids (blue), β-meteoroids (orange), and combined (purple).

UTC and continues until 2020 February 2 8:00 UTC. In this section of the orbit, when the spacecraft has the least amount of roll (i.e., the spacecraft is in a configuration with the $+x$ of the spacecraft frame pointing in the ram direction), a distinct structure becomes apparent forming on the anti-ram side of the histograms. Other time bins (4 and 12 hr) and amplitude bins also exhibit this structure.

Histograms displaying subdivisions of voltage amplitude bins are examined to probe the characteristics of the impactor environment during the anomaly structure. In the full 50–1000 mV window, the anomaly is apparent during all time bins, but that is not the case for the smaller amplitude bins as seen in Figure 5. At the beginning of the anomaly event, the the anomaly structure is not evident in the lowest amplitude bins, 50–100 mV, while it is present in the higher

amplitude bins, 100–200 and 200–400 mV, (see Figure 6). The anomaly continues to be evident in all amplitude bins higher than 100 mV sometime on 2020 January 31 for all time bins. The lower amplitude bin does not present the anomalous structure until 2020 February 1 23:00 UTC and only in the 12 hr time bin where there were sufficient counts to generate a histogram (collecting 97 counts, lower than most 12 hr counts). This low-amplitude histogram indicates a much later start to the anomaly for lower amplitude impactors. It should be noted that this observation may be influenced by the low counts for some of the relevant time stamps at the various amplitude bins.

Figure 5 shows the how the different amplitude windows compare in terms of the count rates as well as with respect to the ram/anti-ram ratios. The window of each plot is centered
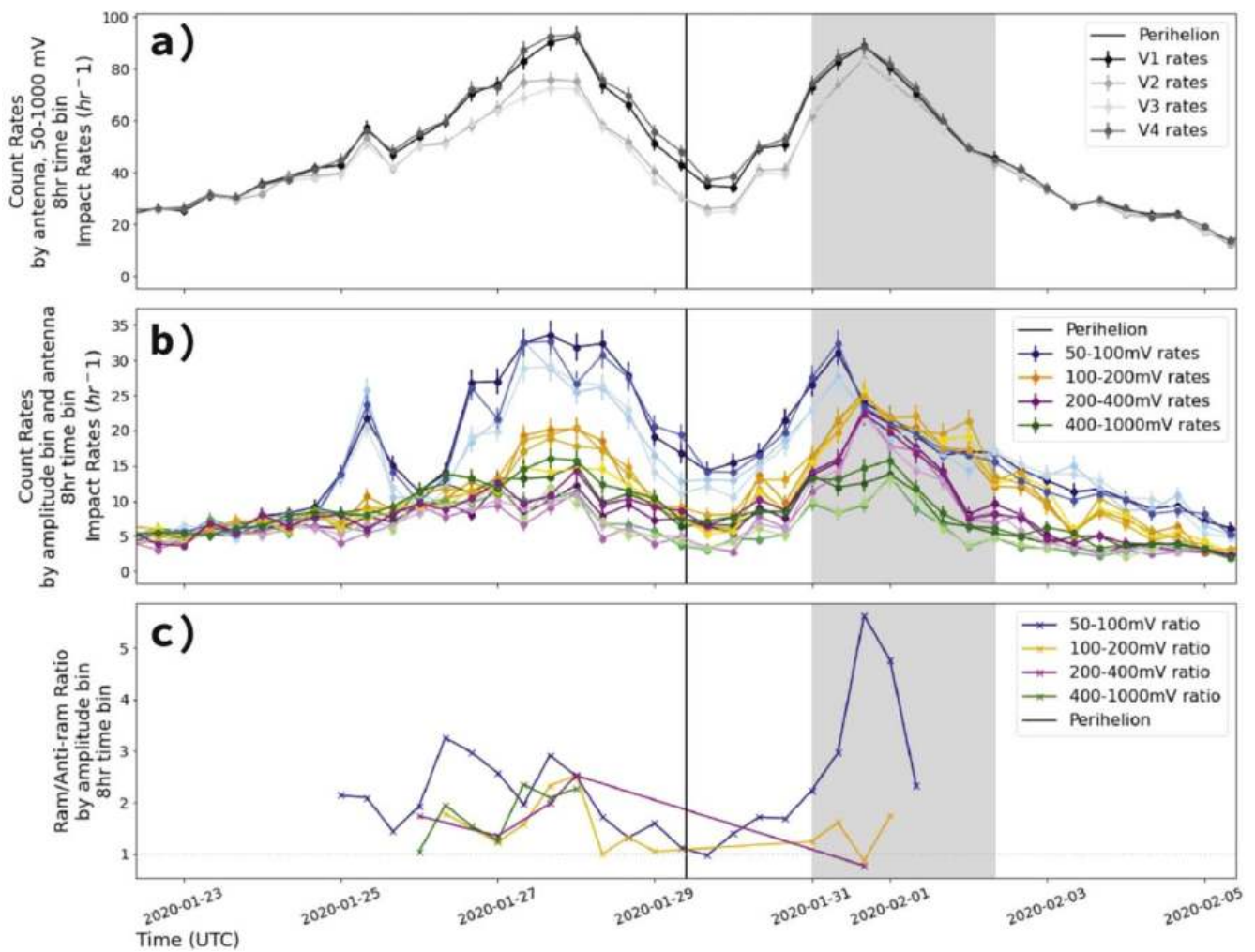
Figure 5. (a): Orbit 4 count rates vs. time for antennas V1, V2, V3, and V4 using the 50–1000 mV amplitude window with darker gray lines corresponding to the ram direction of the spacecraft and lighter gray lines corresponding to the anti-ram direction. (b): Count rates vs. time for each amplitude window on all four planar antennas. Gray shaded region indicates the anomaly duration. (b) carries with it the same gradation as (a) of tone to the various color families depicted, where each color family corresponds to a different amplitude window: blues for 50–100 mV, orange–yellows for 100–200 mV, pinks for 200–400 mV, and greens for 400–1000 mV. (c): Amplitude window ram/anti-ram rates vs. time with the same color families as (b).

on perihelion with about a week to either side, in the section of the orbit without any spacecraft rolls. The top panel shows the Orbit 4 count rates (using the 50–1000 mV amplitude window) versus time with darker gray lines corresponding to the ram direction of the spacecraft (antennas V1 and V4) and lighter gray lines corresponding to the anti-ram direction (V2 and V3). The middle panel carries with it the same gradation of tone to the various color families depicted, where each color family corresponds to a different amplitude window: blues for 50–100 mV, orange–yellows for 100–200 mV, pinks for 200–400 mV, and greens for 400–1000 mV. The bottom panel shows the ram/anti-ram ratios for each amplitude window, following the same color assignments. Not all amplitude windows have data for the entirety of the section depicted. This is due to a lack of sufficient data points in the histograms.

These plots demonstrate that lower amplitude dust detections dominate. In the preperihelion portion of the plot, we see a general trend for all amplitude windows that contribute to the preperihelion peak. Additionally, all amplitude bins see a drop in rates in crossing perihelion, suggesting that the probe travels at a similar relative velocity to the dust in this region of space. The second peak

introduces a new aspect to the anomaly discussed earlier. There is a trend in the rates of the dust amplitudes as the orbit progresses: the beginning of the second peak appears to be composed of small amplitude measurements, then larger, and larger as the peak declines. This structure may hint at the origin of the second peak.

This structure is further expressed when we look at the breakdown of the amplitude windows in the histograms. In a time stamp common to all amplitude windows in the 8 hr time bin (2020 January 31 15:59:50 UTC), there are strong differences among the amplitude windows (Figure 6). In this time stamp, the lower amplitude windows have higher rates, yet they remain distinctly ram-preferential. The anomaly is more prominent in 100–200 and 200–400 mV windows. In the 400–1000 mV range, there were insufficient counts to produce a histogram in the 8 hr interval (68 counts). The anomaly is largely contained in the middle to higher amplitude ranges. Looking at other time stamps in the 12 hr time bin, a wedge does become evident additionally in the 50–100 mV amplitude bin around midnight of 2020 February 1, near the end of the anomaly event.
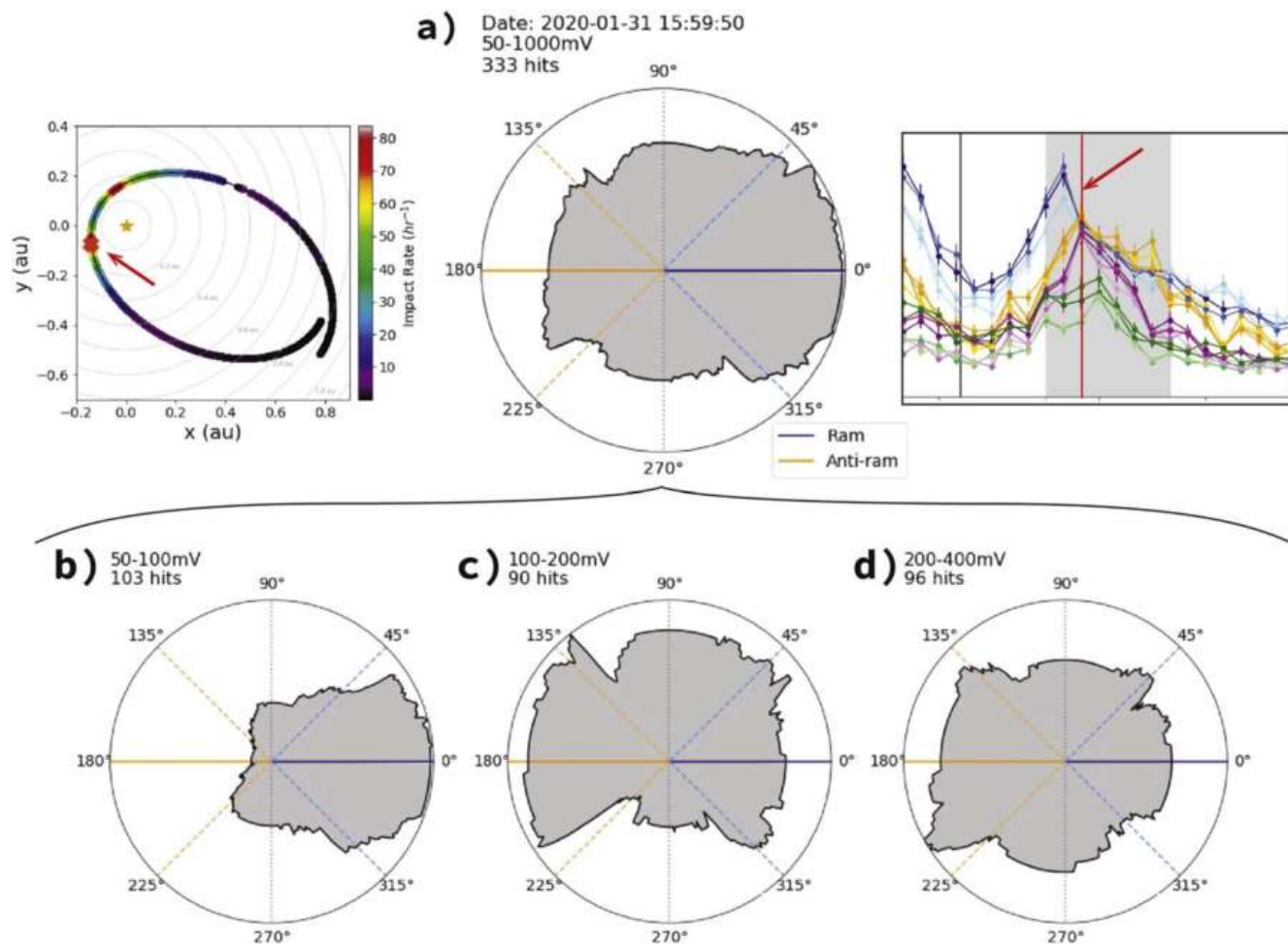
Figure 6. Anomaly as seen in different amplitude windows on 2020 January 31 in an 8 hr time bin starting at about 16:00 UTC. This time bin was chosen because it has statistically significant counts (>75 counts per interval) for most tested amplitude windows during the anomaly. (a) Left: position of spacecraft in orbit 4; middle: full 50–1000 mV amplitude window histogram; right: time stamp of shown histogram in rates as depicted in Figure 5(b). (b)–(d): Same time bin, broken down by amplitude bins: (b) 50–100 mV, (c) 100–200 mV, and (d) 200–400 mV. The 400–1000 mV range is not shown because its counts are <75 (68 count). Notice the extreme ram preference in the low-amplitude ranges and the extreme anti-ram, cone-shaped anomaly in the higher ranges.

4. Discussion

A common feature to all orbital encounters is a peak in the impact rates just before perihelion. This is, along with the general increased rate as the spacecraft speeds up on its approach into perihelion, consistent with orbital models of α- and β-meteoroid populations (Szalay et al. 2021) that show the relative velocity between PSP and dust particles increasing (Figure 4(b)). A combination of increased relative impactor speed and impactor spatial density will cause a larger overall impact flux to PSP. Szalay et al. (2020) constructed models that map the trajectories of various dust populations, including bound α-meteoroids and β-meteoroids with various β values. Using these trajectories, modeled impact rates are produced at various points throughout the spacecraft's orbit. These were compared with FIELDS impact data to determine whether the craft encountered dominantly α-meteoroids on bound orbits, or β-meteoroids on hyperbolic orbits. In Orbit 2, these flux maps were compared with the FIELDS data and Szalay et al. (2020) determined that the impacts on PSP were overwhelmingly due to β-meteoroids rather than α-meteoroids.

When the data from the first three orbits was analyzed, it was posited that the perihelion dip could be evidence of a theorized dust free zone (Mann et al. 2004; Malaspina et al. 2020).

Subsequent orbits have similarly displayed a dip, but the dip appears at lower radii than previous orbits, leading to the strong possibility that this dip is an orbital feature, related to relative velocities between the spacecraft and dust particles rather than the sublimation of dust populations. The dip at perihelion after the initial peak might be explained by the idea that PSP travels with the bound dust particles, encountering them with lower impact speeds, when it is near its closest approach.

The second peak in the postperihelion sections of Orbits 4 and 5, to a lesser extent in Orbit 6, and again in Orbit 7 is a more curious feature. Orbits 1–3 have what might be termed "shoulders," where the decline in the rates is not as steep directly after perihelion. These features seem consistent with models that incorporate both α- and β-meteoroids (see Figure 4(d) Szalay et al. 2021). The lack of a second peak in the first three orbits may be explained by the idea that dust would need to exceed the spacecraft's velocity to produce a high enough amplitude to be included with the 50 mV threshold. But this explanation does not account for the smaller distinct peak in Orbit 6 followed by a prominent second peak in Orbit 7. This distinct double peak in 7 is even more curious then, in addition to the overall increase in count rates within orbit groups. The cause of this second peak in Orbits 4–5 and 7 warrants further investigation.

A retrograde dust population may also be detected by PSP. However, retrograde dust impacts would not produce a second peak and instead would be a single peak centered on perihelion. Such a pattern is not evident in the data. It is assumed that the majority of particles orbit the Sun in prograde orbits. Retrograde populations have significantly shorter collisional lifetimes compared with the prograde population (Steel & Elford 1986). Therefore, it is unlikely the postperihelion peak is due to retrograde particles.

Another possibility is that this is a time-dependent population, for example there might have been a recent collision that created a debris field or meteoroid spray in the vicinity of PSP's postperihelion environment. A very recent or localized collision or break-up of some larger object due to heating or tidal forces might not be expected to produce increased impact rates for both Orbits 4–5 and again in orbit 7. The continued detection of a debris field might depend on how long it takes for the debris to clear in the near-Sun environment, which is outside the scope of this study.

One promising possibility is that PSP is observing another dust population other than the "nominal" zodiacal cloud consisting of azimuthally symmetric α- and β-meteoroids (Szalay et al. 2021). This second peak may be the collisional products, a β-stream, from collisions that occur between the Geminid meteoroid stream and the zodiacal cloud. The Geminid meteor shower is associated with the asteroid 3200 Phaethon which has a very close perihelion distance of 0.14 au to the Sun and and whose dust trail has an inclination angle of about 20° to the ecliptic.[8] While PSP does appear to transit near this trail, determining the absolute fluxes from this collisionally produced dust population requires additional modeling. Specifically, tracking collisionally produced grains with various mass and β values would be key in determining if a β-stream is responsible for the postperihelion anomaly. Referring back to Figure 5, the cascading of amplitude window rates in the postperihelion peak may show the fall off of a β-stream.

The histograms support the β-stream interpretation of the second peak. While the count rates show a cascading in the amplitude bins from low amplitude to high (Figure 5(b)), this picture alone is deceiving because the low-amplitude rates early on correspond to impacts that are distinctly on the ram side of the spacecraft (Figure 6(b).). The wedge shape of the anomaly does not follow the same pattern. Instead, this wedge first appears in the mid- and high-amplitude bins (Figures 6(c) and (d)), and only near the end of the event does it occur in the lower amplitude bins (not shown). This fall off in the amplitude bins of the anomaly in the histograms might indicate a velocity filter. Larger amplitudes could correlate to faster particles which reach PSP ahead of the lower amplitude (i.e., slower particles). This possibility of a velocity filter is limited, however, by the impact charge relation, $Q \propto m^{\alpha} v^{\gamma}$ (Collette et al. 2014). The charge produced by an impacting dust particle is dependent on both the mass and the velocity of the impactor, and these two quantities are not independent of each other. The larger amplitude measurements may be due to larger particles rather than faster particles. However, the exponent on velocity is much larger than on mass, so if the particles were more massive (the difference between the 50–100 mV bin and the

200–400 mV bin), we could no longer consider these particles to be β-meteoroids because the β ratio would become too small.

The data show that smaller amplitude rates occur earlier in the anomaly than larger amplitudes. If these grains are all part of the same population and impact PSP with similar speeds, this would suggest PSP observes increasingly larger impactors as a function of time through the feature and might suggest PSP transited more near to the "core" of the feature toward the end of the anomaly, with the assumption that larger impactors are more central to the population. This interpretations relies on understanding how much the impact velocity vector changes as a function of time over the two to three days this anomaly occurs. It could be that, as PSP's velocity vector rotates even in this three-day period, the impact speeds relative to the source could lead to overall enhanced impact speeds and then charge as a function of time.

If velocity variation primarily determines the shape of the anomaly histograms, the amplitude differences in the time of the directional anomaly along with the time differences for when the anomaly appears at those amplitudes may be used to estimate the relative velocity of the impacting particles. This would correspond to specific β values and could indicate an origin in the Geminids dust trail.

Additionally, the second peak in Orbit 4 corresponds to an increase in the number of counts that cannot be analyzed for directionality using the algorithm described in Section 3.2. If an impact shows its two highest amplitudes on either a V1–V2 or V3–V4 pairing, it is disregarded for the derived directionality histograms. The number of impacts that meet this criteria jump after perihelion from <10% to ~50% of total counts, for an interval that coincides with the postperihelion dust count rate peak in Orbit 4. One possible explanation for these V1–V2 and V3–V4 events may be that dust impacts nearly perpendicular to the heat shield plane (near the center of the heat shield or from the anti-sunward direction) may produce high-amplitude signals on non-adjacent heat shield antennas. In this case, analysis of V5 antenna signals may resolve this mystery. It is also possible that the difference between the second and third highest amplitude measurements could be small for these events, resulting in a assignment of antennas that does not meet our directionality expectations. Although it is unclear why such an effect should be localized to a specific time window after perihelion. In the case that the increase in V1–V2, V3–V4 counts during the second dust count peak is due to dust impacts from the sunward and anti-sunward direction, this observation further support the detection of dust population with unique directionality character, such as the β-stream discussed above.

5. Conclusion

Future analysis will benefit from the subsequent orbits as PSP moves its perihelion closer to the Sun. However, because the all-monopole configuration is not planned for most orbits, an important development of determining dust directionality will be to solidify a method that allows us to extract directionality from dipole data with similar accuracy to the monopole data.

Additional comparison with increasingly realistic models of bound and unbound populations will help to determine if impacts come from one of these populations, or if there might be a third population yet to be discovered, much like the Geminids β-stream possibility (Szalay et al. 2021). Additionally, three-

---

dimensional models will help track β-meteoroid collisional products from the Geminids meteoroid stream. Those models may shed light on what caused both the peak in the count rates and the anomaly in the directionality histograms.

Another avenue of study would be to compare known dust impacts with WISPR (the white light telescope on PSP; Vourlidas et al. 2016) images that were taken at the same time as the impact to see if the locations of dust impacts on the spacecraft can be discerned and to compare with dust number densities derived by combining observed dust count rates and dust dynamics modeling. The field of view of WISPR is limited to one side (ram) of the spacecraft, but analysis of WISPR images will give another dimension to impact analysis. Further, WISPR has imaged the Geminids trail (Battams et al. 2020). Corroborating its location with the position of PSP might reveal what we see in the data.

Analysis of cyclotron wave frequencies that have been shown to accompany some dust impacts (Tsurutani & Smith 1986; Tsurutani et al. 1995) could also offer interesting insight into the material impacting the spacecraft.

One more element not explored here but potentially helpful for understanding dust directionality is to incorporate data from V5. The spacecraft not only rolls around its axis, but it also off points away from the Sun, that is, the $+z$ in the spacecraft frame deviates from the radial direction toward the Sun (Figure 3). This only happens when the spacecraft is far from perihelion. In this way, changes in PSP's orientation can help further elucidate the direction of dust impacts, and might also reintroduce data that had been set aside because the two highest amplitude detections were on opposing antennas in the plane of the heat shield. V5 data may show that such measurements were due to dust impacts on the back of the craft.

ORCID iDs

A. Pusack https://orcid.org/0000-0002-3081-8597
D. M. Malaspina https://orcid.org/0000-0003-1191-1558
J. R. Szalay https://orcid.org/0000-0003-2685-9801
S. D. Bale https://orcid.org/0000-0002-1989-3596
Keith Goetz https://orcid.org/0000-0003-0420-3633
Robert J. MacDowall https://orcid.org/0000-0003-3112-4201
Marc Pulupa https://orcid.org/0000-0002-1573-7457

References

Andersson, L., Weber, T. D., Malaspina, D. M., et al. 2015, Sci, 350, 0398
Bale, S. D., Goetz, K., Bonnell, J. W., et al. 2020, arXiv:2006.00776
Bale, S. D., Goetz, K., Harvey, P. R., et al. 2016, SSRv, 204, 49
Battams, K., Knight, M. M., Kelley, M. S. P., et al. 2020, ApJS, 246, 64
Collette, A., Grün, E., Malaspina, D., & Sternovsky, Z. 2014, JGRA, 119, 6019
Collette, A., Malaspina, D. M., & Sternovsky, Z. 2016, JGRA, 121, 8182
Collette, A., Meyer, G., Malaspina, D. M., & Sternovsky, Z. 2015, JGRA, 120, 5298
Dorschner, J. 2001, Interplanetary Dust (Berlin: Springer), 727
Fox, N., Velli, M. C., Bale, S. D., et al. 2016, SSRv, 204, 7
Grün, E., Krüger, H., & Srama, R. 2019, SSRv, 215, 46
Grün, E., Zook, H., Fechtig, H., & Giese, R. 1985, Icar, 62, 244
Gurnett, D. A., Averkamp, T. F., Scarf, F. L., & Grun, E. 1986, GeoRL, 13, 291
Kellogg, P. J., Goetz, K., & Monson, S. J. 2016, JGRA, 121, 966
Koschny, D., Soja, R. H., Engrand, C., et al. 2019, SSRv, 215, 34
Krivov, A. V., Mann, I., & Krivova, N. A. 2000, A&A, 362, 1127
Krüger, H., Grün, P. S. E., & Sterken, V. J. 2015, ApJ, 812, 139
Krüger, H., Strub, P., Altobelli, N., et al. 2019, A&A, 626, A37
Laakso, H., Grard, R., Pedersen, A., & Schwehm, G. 1989, AdSpR, 9, 269
Malaspina, D. M., Horanyi, M., Zaslavsky, A., et al. 2014, GeoRL, 41, 266
Malaspina, D. M., Szalay, J. R., Pokorný, P., et al. 2020, ApJ, 892, 115
Mann, I., Kimura, H., Biesecker, D. A., et al. 2004, SSRv, 110, 269
Mann, I., Nouzák, L., Vaverka, J., et al. 2019, AnGeo, 37, 1121
McNutt, R. L., Wimmer-Schweingruber, R. F., Gruntman, M., et al. 2019, AcAau, 162, 284
Meyer-Vernet, N., Maksimovic, M., Czechowski, A., et al. 2009, SoPh, 256, 463
Nouzák, L., Hsu, S., Malaspina, D., et al. 2018, P&SS, 156, 85
Page, B., Bale, S. D., Bonnell, J. W., et al. 2020, ApJS, 246, 51
Shen, M., Sternovsky, Z., Garzelli, A., & Malaspina, D. M. 2021a, Earth and Space Science Open Archive, doi:10.1002/essoar.10507271.1
Shen, M. M., Sternovsky, Z., Horányi, M., Hsu, H.-W., & Malaspina, D. M. 2021b, JGRA, 126, e28965
Steel, D. I., & Elford, W. G. 1986, MNRAS, 218, 185
Szalay, J. R., Pokorný, P., Bale, S. D., et al. 2020, ApJS, 246, 27
Szalay, J. R., Pokorny, P., Malaspina, D. M., et al. 2021, PSJ, 2, 185
Tsurutani, B. T., Clay, D. R., Zhang, L. D., et al. 2003, GeoRL, 30, 2134
Tsurutani, B. T., Clay, D. R., Zhang, L. D., et al. 2004, Icar, 167, 89
Tsurutani, B. T., Glassmeier, K. H., & Neubauer, F. M. 1995, GeoRL, 22, 1149
Tsurutani, B. T., & Smith, E. J. 1986, GeoRL, 13, 263
Vaverka, J., Nakamura, T., Kero, J., et al. 2018, JGRA, 123, 6119
Vaverka, J., Pavlů, J., Nouzák, L., et al. 2019, JGRA, 124, 8179
Vourlidas, A., Howard, R. A., Plunkett, S. P., et al. 2016, SSRv, 204, 83
Ye, S.-Y., Gurnett, D. A., Kurth, W. S., et al. 2014, JGRA, 119, 6294
Zaslavsky, A., Meyer-Vernet, N., Mann, I., et al. 2012, JGRA, 117, A05102
Zook, H. A., & Berg, O. E. 1975, P&SS, 23, 183